Two-step Perfectly Matched Layer for Arbitrary-Order Pseudo-Spectral Analytical Time-Domain Methods

Olga Shapoval[a,*], Jean-Luc Vay[a], Henri Vincenti[b]

[a] *Lawrence Berkeley National Laboratory, Berkeley, CA 94720, USA*
[b] *LIDYL, CEA, CNRS, Universite Paris-Saclay, CEA Saclay, 91 191 Gif-sur-Yvette, France*

Abstract

Numerical simulation of an electrodynamic system in empty space requires the implementation of open boundary conditions (BC) to terminate the solution of Maxwell's equations on the boundaries of the computational domain. The Perfectly Matched Layer (PML) has become the method of choice for open BC with wave equations, as it is straightforward and relatively easy to implement, and offers very efficient and user-adjustable absorption rates. PMLs are most often employed with the Finite-Difference Time-Domain (FDTD) algorithm, which in its most common implementation offers second-order accuracy in space and time on Cartesian grids. Yet, simulations (including some class of electromagnetic Particle-In-Cell simulations) that require higher precision may resort to higher-order Maxwell solvers employing extended finite-difference stencils, or even to pseudo-spectral Maxwell solvers, for which a general, versatile and efficient formulation of the PML has been missing so far. In this paper, we propose a novel "two-step" formulation of the PML that is simple, very versatile and can be used as is with any Maxwell solver. In particular, it is applicable to a large class of Maxwell solvers including the arbitrary-order Pseudo-Spectral Analytical Time-Domain (PSATD) solver, which offers arbitrarily low numerical dispersion when increasing solver order and becomes dispersion-free at infinite order. Analysis and numerical simulations demonstrate that the new formulation is as efficient as the standard PML formulation, both for the FDTD and the PSATD implementations.

Keywords: perfectly matched layer; PML; asymmetric perfectly matched layer; APML; finite-difference time-domain method; FDTD; pseudo-spectral time domain method; PSTD; pseudo-spectral analytical time domain method; PSATD; Maxwell's equations;

1. Introduction

The Finite-Difference Time-Domain (FDTD) (which includes "Yee's method") [1] is one of the most popular methods for solving Maxwell's equations. It operates second-order finite differences in time and space to advance electromagnetic fields that are defined on a staggered grid. Apart from its second order convergence properties, the main advantages of the Yee's scheme stem from its time-reversibility and energy conservation, as well as its spatial locality,

*Corresponding author.
E-mail address: oshapoval@lbl.gov (O. Shapoval), jlvay@lbl.gov (J.-L. Vay)

which allows for simple parallel distributed implementations that already demonstrated good scalability to millions of CPU cores. For some applications, however, the numerical dispersion of electromagnetic (EM) waves with the FDTD solver leads to unacceptable levels of numerical errors, whose mitigation requires very small grid sizes that are not tractable, even on modern supercomputers [2, 3, 4, 5]. For those applications, higher-order solvers, including FFT-based Pseudo-Spectral Time-Domain (PSTD) and Pseudo-Spectral Analytical Time-Domain (PSATD) methods, are being used [6, 7]. The PSATD method [7], in particular, integrates Maxwell's equations analytically in Fourier space, and is thus free of numerical dispersion and Courant condition. While the extension of the Perfectly Matched Layer (PML) [8, 9] method (to simulate open systems) to PSTD is straightforward [10], its application to PSATD demands a different and more general formulation.

In this context, the goal of this paper is to present a novel "two-step" PML method that can be applied to any type of very-high order/pseudo-spectral solvers, including the so-called PSATD solver. The new method is introduced first as a subset of the Asymmetric Perfectly Matched Layer (APML) for the second-order FDTD scheme, then extended to arbitrary order, up to infinite-order PSTD, and finally to the PSATD solver (at any order).

The paper is structured as follows. Section II recalls and summarizes the definition of the APML. Section III first introduces two forms of the "two-step" formulation for the FDTD algorithm: time-staggered "PML-2SS" and time-centered "PML-2SC". It then extends this formulation to arbitrary-order finite-difference solvers, as well as to PSTD and PSATD solvers. Section IV analyzes the numerical dispersion of the two formulations and contrasts them to the standard PML's. Section V compares the absorption rate of the new formulations with Berenger's PML for an incident plane wave at various wavelengths (normalized by cell size) and incidence angles, obtained via numerical simulations or analytically. Section VI presents results from electromagnetic Particle-In-Cell simulations of plasma-laser interactions at ultra-high intensities that were enabled by: (i) using the ultrahigh-order pseudo-spectral PSATD solver to mitigate spurious numerical dispersion effects over large bands of frequencies and angles, and (ii) use of the new two-step PML to avoid spurious reflections of the high-intensity electromagnetic fields (incident and reflected fields) at the simulation domain boundaries. Conclusions are summarized in Section VII.

2. Asymmetric Perfectly Matched Layer (APML)

Without loss of generality and for the sake of simplicity, let us consider the propagation of the transverse electric waves (TE mode) in free space, where the electromagnetic field has only three non-zero components E_x, E_y, H_z, with z chosen along the direction of propagation (see Fig. 1 (a)). In two dimensions, an APML medium (in normalized units) can be introduced as a generalization of the Berenger's PML medium [8, 9], by adding additional constraints to the

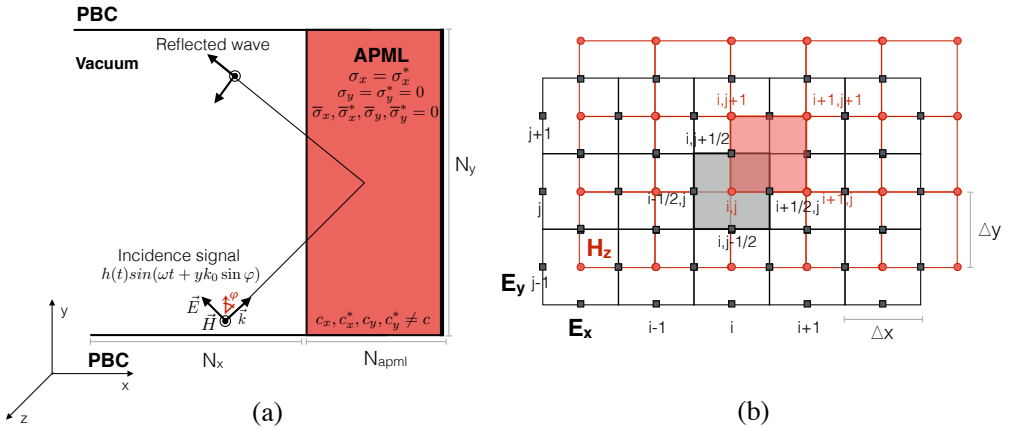

Figure 1: (a) Schematic 2D representation of the TE plane-wave striking right-hand APML medium of the depth N_{apml} together with periodic boundary conditions (PBC) at upper and lower boundaries. (b) Two-dimensional spatial arrangement of **E** and **H** field components on the "Yee" staggered grid.

split-form of Maxwell's equations in the form of extra coefficients and extra terms [11, 12]:

$$\frac{\partial E_x}{\partial t} + \sigma_y E_x = \frac{c_y}{c}\frac{\partial H_z}{\partial y} + \overline{\sigma}_y H_z, \tag{1}$$

$$\frac{\partial E_y}{\partial t} + \sigma_x E_y = -\frac{c_x}{c}\frac{\partial H_z}{\partial x} + \overline{\sigma}_x H_z, \tag{2}$$

$$\frac{\partial H_{zx}}{\partial t} + \sigma_x^* H_{zx} = -\frac{c_x^*}{c}\frac{\partial E_y}{\partial x} + \overline{\sigma}_x^* E_y, \tag{3}$$

$$\frac{\partial H_{zy}}{\partial t} + \sigma_y^* H_{zy} = \frac{c_y^*}{c}\frac{\partial E_x}{\partial y} + \overline{\sigma}_y^* E_x, \tag{4}$$

$$H_z = H_{zx} + H_{zy}. \tag{5}$$

Here, (σ_x, σ_y) and (σ_x^*, σ_y^*) are electric and magnetic conductivities, while c is the speed of light in vacuum. In contrast to the Berenger's PML medium, such formulation introduces: (i) counterpart of the electric and magnetic conductivities $(\overline{\sigma}_x, \overline{\sigma}_y)$ and $(\overline{\sigma}_x^*, \overline{\sigma}_y^*)$ affecting the right part of the Eqs. (1)-(4); (ii) coefficients (c_x, c_y) and (c_x^*, c_y^*), by which phase velocity is multiplied in each direction.

It was shown [12] that the APML medium is a PML, with asymmetry in the absorption rate for some settings of the extra parameters (hence, the etymology of Asymmetric PML). The APML absorbs electromagnetic waves at any wavelength and incidence angle if $c_x = c_x^*$, $c_y = c_y^*$, $\overline{\sigma}_x = \overline{\sigma}_x^*$, $\overline{\sigma}_y = \overline{\sigma}_y^*$, $\sigma_x = \sigma_x^*$ and $\sigma_y = \sigma_y^*$. If $c_x = c_y = c_x^* = c_y^* = c$ and $\overline{\sigma}_x = \overline{\sigma}_y = \overline{\sigma}_x^* = \overline{\sigma}_y^* = 0$, Eqs. (1)-(5) reduce to the original Berenger's PML medium, and if, in addition, $\sigma_x = \sigma_x^* = \sigma_y = \sigma_y^* = 0$ the system of Eqs. (1)-(5) reduces to the Maxwell's equations in vacuum.

In [12], the absorbing properties of the APML were analyzed when $c_x = c_y = c_x^* = c_y^* = c$ and $\overline{\sigma}_x = \overline{\sigma}_y = \overline{\sigma}_x^* = \overline{\sigma}_y^* \neq 0$. In this paper, we will focus on the special case where $\overline{\sigma}_x = \overline{\sigma}_y = \overline{\sigma}_x^* = \overline{\sigma}_y^* = 0$ and $c_x = c_y = c_x^* = c_y^* \neq c$. Specific values of the phase velocity coefficients will be chosen so as to introduce a novel "2-step" formulation of PML that is devised for application to the PSATD Maxwell solver [7, 13].

3. Discretization of the PML

As a discrete space, we assume the "Yee" grid staggered in space and time [1] (note that application of the methods presented below can be readily extended to the discretization on a nodal grid). The spatial layout of the **E** and **H** field-components is shown in Fig. 1 (b).

3.1. Standard second-order FDTD discretization

The standard second-order FDTD discretization of Eqs. (1)-(5), using exponential time-stepping, writes (assuming $\overline{\sigma}_x = \overline{\sigma}_y = \overline{\sigma}^*_x = \overline{\sigma}^*_y = 0$),

$$H_{zx}|^{n+1/2}_{i+1/2,j+1/2} = e^{-\sigma^*_x \Delta t} H_{zx}|^{n-1/2}_{i+1/2,j+1/2} - \frac{1-e^{-\sigma^*_x \Delta t}}{\sigma^*_x \Delta x} \frac{c^*_x}{c} \left(E_y|^{n+1}_{j+1,k+1/2} - E_y|^{n+1}_{j,k+1/2} \right), \quad (6)$$

$$H_{zy}|^{n+1/2}_{i+1/2,j+1/2} = e^{-\sigma^*_y \Delta t} H_{zy}|^{n-1/2}_{i+1/2,j+1/2} + \frac{1-e^{-\sigma^*_y \Delta t}}{\sigma^*_y \Delta y} \frac{c^*_y}{c} \left(E_x|^{n+1}_{i+1/2,j+1} - E_x|^{n+1}_{i+1/2,j} \right), \quad (7)$$

$$E_x|^{n+1}_{i+1/2,j} = e^{-\sigma_y \Delta t} E_x|^{n}_{i+1/2,j} + \frac{1-e^{-\sigma_y \Delta t}}{\sigma_y \Delta y} \frac{c_y}{c} \left(H_z|^{n+1/2}_{i+1/2,j+1/2} - H_z|^{n+1/2}_{i+1/2,j-1/2} \right), \quad (8)$$

$$E_y|^{n+1}_{i,j+1/2} = e^{-\sigma_x \Delta t} E_y|^{n}_{i,j+1/2} - \frac{1-e^{-\sigma_x \Delta t}}{\sigma_x \Delta x} \frac{c_x}{c} \left(H_z|^{n+1/2}_{i+1/2,j+1/2} - H_z|^{n+1/2}_{i-1/2,j+1/2} \right), \quad (9)$$

where Δx and Δy denote the spatial cell size along x and y respectively, and Δt corresponds to the time increment. The pair of subindices (i, j) denotes the center positions of the spatial cells (see Fig. 1(b)), while the time step is denoted by integer superindex n.

Note that when $c_x = c^*_x = c_y = c^*_y = c$, Eqs. (6)-(9) become the second-order FDTD discretization of the standard Berenger's PML formulation, using exponential time-stepping.

3.2. Novel two-step discretization

We now set the coefficients c_x, c_y, c^*_x, and c^*_y so as to derive a novel "two-step" formulation of the PML. For convenience, let us introduce the notation $c^{(*)}_x$, in which the superscript (*) unites the definitions of the coefficients with and without star (namely, c_x and c^*_x).

Assuming the special choice of the coefficients $c^{(*)}_x$ and $c^{(*)}_y$:

$$c^{(*)}_x = c e^{-\sigma^{(*)}_x \Delta t} \frac{\sigma^{(*)}_x \Delta t}{1-e^{-\sigma^{(*)}_x \Delta t}}, \quad (10)$$

$$c^{(*)}_y = c e^{-\sigma^{(*)}_y \Delta t} \frac{\sigma^{(*)}_y \Delta t}{1-e^{-\sigma^{(*)}_y \Delta t}}, \quad (11)$$

the resulting second-order FDTD discretization writes:

$$H_{zx}|^{n+1/2}_{i+1/2,j+1/2} = e^{-\sigma^*_x \Delta t} \Big[H_{zx}|^{n-1/2}_{i+1/2,j+1/2} - \frac{\Delta t}{\Delta x} \Big(E_y|^{n}_{i+1,j+1/2} - E_y|^{n}_{i,j+1/2} \Big) \Big], \quad (12)$$

$$H_{zy}|^{n+1/2}_{i+1/2,j+1/2} = e^{-\sigma^*_y \Delta t} \Big[H_{zy}|^{n-1/2}_{i+1/2,j+1/2} + \frac{\Delta t}{\Delta y} \Big(E_x|^{n}_{i+1/2,j+1} - E_x|^{n}_{i+1/2,j} \Big) \Big], \quad (13)$$

$$E_x|^{n+1}_{i+1/2,j} = e^{-\sigma_y \Delta t} \Big[E_x|^{n}_{i+1/2,j} + \frac{\Delta t}{\Delta y} \Big(H_z|^{n+1/2}_{i+1/2,j+1/2} - H_z|^{n+1/2}_{i+1/2,j-1/2} \Big) \Big], \quad (14)$$

$$E_y|^{n+1}_{i,j+1/2} = e^{-\sigma_x \Delta t} \Big[E_y|^{n}_{i,j+1/2} - \frac{\Delta t}{\Delta x} \Big(H_z|^{n+1/2}_{i+1/2,j+1/2} - H_z|^{n+1/2}_{i-1/2,j+1/2} \Big) \Big]. \quad (15)$$

Note that at infinitesimal limit $c^{(*)}_x, c^{(*)}_y \to c$ when $\Delta t \to 0$.

3.2.1. Two-step time-staggered PML ("PML-2SS")

This choice of coefficients enables a rewrite of the PML update as a two-step process

$$\widetilde{H}_{zx}|^{n+1/2}_{i+1/2,j+1/2} = H_{zx}|^{n-1/2}_{i+1/2,j+1/2} - \frac{\Delta t}{\Delta x}\Big(E_y|^{n}_{i+1,j+1/2} - E_y|^{n}_{i,j+1/2}\Big), \tag{16}$$

$$\widetilde{H}_{zy}|^{n+1/2}_{i+1/2,j+1/2} = H_{zy}|^{n-1/2}_{i+1/2,j+1/2} + \frac{\Delta t}{\Delta y}\Big(E_x|^{n}_{i+1/2,j+1} - E_x|^{n}_{i+1/2,j}\Big), \tag{17}$$

$$H_{zx}|^{n+1/2}_{i+1/2,j+1/2} = e^{-\sigma^*_x \Delta t}\widetilde{H}_{zx}|^{n+1/2}_{i+1/2,j+1/2}, \tag{18}$$

$$H_{zy}|^{n+1/2}_{i+1/2,j+1/2} = e^{-\sigma^*_y \Delta t}\widetilde{H}_{zy}|^{n+1/2}_{i+1/2,j+1/2}, \tag{19}$$

$$\widetilde{E}_x|^{n+1}_{i+1/2,j} = E_x|^{n}_{i+1/2,j} + \frac{\Delta t}{\Delta y}\Big(H_z|^{n+1/2}_{i+1/2,j+1/2} - H_z|^{n+1/2}_{i+1/2,j-1/2}\Big), \tag{20}$$

$$\widetilde{E}_y|^{n+1}_{i,j+1/2} = E_y|^{n}_{i,j+1/2} - \frac{\Delta t}{\Delta x}\Big(H_z|^{n+1/2}_{i+1/2,j+1/2} - H_z|^{n+1/2}_{i-1/2,j+1/2}\Big), \tag{21}$$

$$E_x|^{n+1}_{i+1/2,j} = e^{-\sigma_y \Delta t}\widetilde{E}_x|^{n+1}_{i+1/2,j}, \tag{22}$$

$$E_y|^{n+1}_{i,j+1/2} = e^{-\sigma_x \Delta t}\widetilde{E}_y|^{n+1}_{i,j+1/2}. \tag{23}$$

where the magnetic and electric components are first pushed in vacuum, then scaled respectively after each individual push in vacuum by $e^{-\sigma^*_u \Delta t}$ and $e^{-\sigma_u \Delta t}$ in the direction u, for **E** and **H**, respectively.

3.2.2. Two-step time-centered PML ("PML-2SC")

An alternate formulation is based on a time-centered push of the field components in vacuum, followed by the synchronized scaling of all the components

$$\widetilde{H}_{zx}|^{n+1/2}_{i+1/2,j+1/2} = H_{zx}|^{n}_{i+1/2,j+1/2} - 0.5\frac{\Delta t}{\Delta x}\Big(E_y|^{n}_{i+1,j+1/2} - E_y|^{n}_{i,j+1/2}\Big), \tag{24}$$

$$\widetilde{H}_{zy}|^{n+1/2}_{i+1/2,j+1/2} = H_{zy}|^{n}_{i+1/2,j+1/2} + 0.5\frac{\Delta t}{\Delta y}\Big(E_x|^{n}_{i+1/2,j+1} - E_x|^{n}_{i+1/2,j}\Big), \tag{25}$$

$$\widetilde{E}_x|^{n+1}_{i+1/2,j} = E_x|^{n}_{i+1/2,j} + \frac{\Delta t}{\Delta y}\Big(\widetilde{H}_z|^{n+1/2}_{i+1/2,j+1/2} - \widetilde{H}_z|^{n+1/2}_{i+1/2,j-1/2}\Big), \tag{26}$$

$$\widetilde{E}_y|^{n+1}_{i,j+1/2} = E_y|^{n}_{i,j+1/2} - \frac{\Delta t}{\Delta x}\Big(\widetilde{H}_z|^{n+1/2}_{i+1/2,j+1/2} - \widetilde{H}_z|^{n+1/2}_{i-1/2,j+1/2}\Big), \tag{27}$$

$$\widetilde{H}_{zx}|^{n+1}_{i+1/2,j+1/2} = \widetilde{H}_{zx}|^{n+1/2}_{i+1/2,j+1/2} - 0.5\frac{\Delta t}{\Delta x}\Big(\widetilde{E}_y|^{n+1}_{i+1,j+1/2} - \widetilde{E}_y|^{n}_{i,j+1/2}\Big), \tag{28}$$

$$\widetilde{H}_{zy}|^{n+1}_{i+1/2,j+1/2} = \widetilde{H}_{zy}|^{n+1/2}_{i+1/2,j+1/2} + 0.5\frac{\Delta t}{\Delta y}\Big(\widetilde{E}_x|^{n}_{i+1/2,j+1} - \widetilde{E}_x|^{n}_{i+1/2,j}\Big), \tag{29}$$

$$H_{zx}|^{n+1}_{i+1/2,j+1/2} = e^{-\sigma^*_x \Delta t}\widetilde{H}_{zx}|^{n+1}_{i+1/2,j+1/2}, \tag{30}$$

$$H_{zy}|^{n+1}_{i+1/2,j+1/2} = e^{-\sigma^*_y \Delta t}\widetilde{H}_{zy}|^{n+1}_{i+1/2,j+1/2}, \tag{31}$$

$$E_x|^{n+1}_{i+1/2,j} = e^{-\sigma_y \Delta t}\widetilde{E}_x|^{n+1}_{i+1/2,j}, \tag{32}$$

$$E_y|^{n+1}_{i,j+1/2} = e^{-\sigma_x \Delta t}\widetilde{E}_y|^{n+1}_{i,j+1/2}. \tag{33}$$

That is, at each time step, the field components **E** and **H** are updated in the following order:

- solve Maxwell's equations in vacuum over one time step;

- multiply updated field components by the corresponding PML's damping coefficients $e^{-\sigma_u^{(*)}\Delta t}$.

By recasting the PML formulation in (i) a standard Maxwell push in vacuum and (ii) a simple field damping in the PML, this two-step technique is very versatile and can be used as is with any Maxwell solver for step (i) and without re-writing discretized equations for the PMLs.

3.3. Extension to High-order and Fourier-based Discretization

The PML-2SS and PML-2SC algorithms can be easily extended to other Maxwell solvers, by simply replacing the first step of propagation in vacuum (the second damping step remaining unchanged). Below, we briefly review different classes of Maxwell solvers that can be used in the Maxwell push step of the two-step model and whose effect on the APML efficiency will be tested in the section 5 of this manuscript.

3.3.1. High-Order Spatial Finite-Difference

The discrete finite-difference operator of the spatial derivative of p-order on staggered "Yee" grid writes:

$$\frac{\partial f_{i,j}}{\partial u} \approx \sum_{l=1}^{p/2} c_l^p \frac{(f_{i+l-1,j} - f_{i-l,j})}{\Delta u}, \quad u = \{x, y\} \tag{34}$$

where $c_l^p, l = 1, 2, ..., p/2$ are known as Fornberg coefficients [14], calculated by the Taylor expansion-based closed-form formulas [15], and given for a staggered grid by [16]:

$$c_l^p = \frac{(-1)^{l+1} 16^{1-p/2} (p-1)!^2}{(2l-1)^2 (p/2+l-1)!(p/2-l)!(p/2-1)!^2}, \quad l = 1, 2, ..., p/2. \tag{35}$$

An arbitrary p-order discretization of the split-form of Maxwell's equations in vacuum is thus given by

$$H_{zx}|_{i+1/2,j+1/2}^{n+1/2} = H_{zx}|_{i+1/2,j+1/2}^{n-1/2} - \frac{\Delta t}{\Delta x} \sum_{l=1}^{p/2} c_l^p \Big(E_y|_{i+l,j+1/2}^{n} - E_y|_{i-(l-1),j+1/2}^{n} \Big), \tag{36}$$

$$H_{zy}|_{i+1/2,j+1/2}^{n+1/2} = H_{zy}|_{i+1/2,j+1/2}^{n-1/2} + \frac{\Delta t}{\Delta y} \sum_{l=1}^{p/2} c_l^p \Big(E_x|_{i+1/2,j+1+l}^{n} - E_x|_{i+1/2,j-(l-1)}^{n} \Big), \tag{37}$$

$$E_x|_{i+1/2,j}^{n+1} = E_x|_{i+1/2,j}^{n} + \frac{\Delta t}{\Delta y} \sum_{l=1}^{p/2} c_l^p \Big(H_z|_{i+1/2+(l-1),j+1/2}^{n+1/2} - H_z|_{i+1/2-l,j-1/2}^{n+1/2} \Big), \tag{38}$$

$$E_y|_{i,j+1/2}^{n+1} = E_y|_{i,j+1/2}^{n} - \frac{\Delta t}{\Delta x} \sum_{l=1}^{p/2} c_l^p \Big(H_z|_{i+1/2,j+1/2+(l-1)}^{n+1/2} - H_z|_{i-1/2,j+1/2-l}^{n+1/2} \Big). \tag{39}$$

Equations (36)-(39) can be used in place of the corresponding second-order Maxwell FDTD equations in vacuum in the PML-2SS and PML-2SC algorithms.

3.3.2. Pseudo-Spectral Time-Domain Discretization

The Pseudo-Spectral Time-Domain (PSTD) method is based on solving Maxwell's equations by advancing electromagnetic fields in Fourier space (**k**-space), while second-order time Leapfrog differentiation is retained in real space [17, 6, 10]. The field derivative with respect to the spatial coordinate u ($u = x$ or y) is evaluated in Fourier space

$$\frac{\partial f(u)}{\partial u} = \frac{\partial}{\partial u}\int_{-\infty}^{\infty} \mathcal{F}[f(u)]e^{ik_u u}dk_u = \mathcal{F}^{-1} ik_u \mathcal{F}[f(u)] \tag{40}$$

where $\mathcal{F}$ and $\mathcal{F}^{-1}$ denote the forward and inverse Fourier transforms, respectively; **k** is the wavevector of length $k = (k_x^2 + k_y^2 + k_z^2)^{1/2}$. We note that the derivative evaluated in Fourier space by Eq. (40) is the limit of finite-difference at order p (Eq. (34)) when $p \to \infty$.

The extension of Eq. (40) to arbitrary finite-order p is given by representing $\nabla^p f$ in terms of the Fourier integral, and further applying the convolution theorem, giving

$$\frac{\partial f(u)}{\partial u} = \mathcal{F}^{-1} i[k_u]_p \mathcal{F}[f(u)], \tag{41}$$

$$[k_u]_p = \frac{2}{\Delta u}\sum_{l=1}^{p/2} c_l^p \sin\Big((2l-1)\frac{k_u \Delta u}{2}\Big), \tag{42}$$

where $[k_u]_p$, with $u = (x \text{ or } y)$, corresponds to the p-order wavenumber components.

Following the notation used in the previous subsections and by applying spatial Fourier transforms, the split-form of Maxwell equations in vacuum at order p is reformulated as follows,

$$H_{zx}|^{n+1/2}_{i+1/2,j+1/2} = H_{zx}|^{n-1/2}_{i+1/2,j+1/2} - \Delta t\Big(\mathcal{F}^{-1} i[k_x] e^{ik_x \Delta x/2}\mathcal{F}\Big(E_y|^n_{i+1/2,j+1/2}\Big)\Big), \tag{43}$$

$$H_{zy}|^{n+1/2}_{i+1/2,j+1/2} = H_{zy}|^{n-1/2}_{i+1/2,j+1/2} + \Delta t\Big(\mathcal{F}^{-1} i[k_y] e^{ik_y \Delta y/2}\mathcal{F}\Big(E_x|^n_{i+1/2,j+1/2}\Big)\Big), \tag{44}$$

$$E_x|^{n+1}_{i+1/2,j} = E_x|^n_{i+1/2,j} + \Delta t\Big(\mathcal{F}^{-1} i[k_y] e^{-ik_y \Delta y/2}\mathcal{F}\Big(H_z|^{n+1/2}_{i+1/2,j}\Big)\Big), \tag{45}$$

$$E_y|^{n+1}_{i,j+1/2} = E_y|^n_{i,j+1/2} - \Delta t\Big(\mathcal{F}^{-1} i[k_x] e^{-ik_x \Delta x/2}\mathcal{F}\Big(H_z|^{n+1/2}_{i,j+1/2}\Big)\Big). \tag{46}$$

Here, the terms $e^{ik_x \Delta x/2}$ and $e^{ik_y \Delta y/2}$ correspond to the space shifts along x and y axes on the staggered "Yee" grid for E_y, while $e^{-ik_x \Delta x/2}$ and $e^{-ik_y \Delta y/2}$ are the shifts for H_z [10].

Equations (43)-(46) can be used in place of the corresponding second-order Maxwell FDTD equations in vacuum in the PML-2SS and PML-2SC algorithms, and are more advantageous, in term of computational cost, than their finite-difference counterpart for simulations that require high-order accuracy [18].

3.3.3. Pseudo-Spectral Analytical Time-Domain Discretization

Maxwell's equations in vacuum can be integrated analytically in Fourier space over one time step, provided that the source terms are constant over the time interval [7, 13]. The resulting algorithm is given by (omitting the source terms):

$$H_{zx}|^{n+1}_{i+1/2,j+1/2} = \mathcal{F}^{-1} C\Big(\mathcal{F} H_{zx}|^n_{i+1/2,j+1/2}\Big) - \Big(\mathcal{F}^{-1} iS\hat{k}_x e^{ik_x \Delta y/2}\Big(\mathcal{F} E_y|^n_{i+1/2,j+1/2}\Big)\Big), \tag{47}$$

$$H_{zy}|^{n+1}_{i+1/2,j+1/2} = \mathcal{F}^{-1} C\Big(\mathcal{F} H_{zy}|^n_{i+1/2,j+1/2}\Big) + \Big(\mathcal{F}^{-1} iS\hat{k}_y e^{ik_y \Delta y/2}\Big(\mathcal{F} E_x|^n_{i+1/2,j+1/2}\Big)\Big), \tag{48}$$

$$E_x|^{n+1}_{i+1/2,j} = \mathcal{F}^{-1} C\Big(\mathcal{F} E_x|^n_{i+1/2,j}\Big) + \Big(\mathcal{F}^{-1} iS\hat{k}_y e^{-ik_y \Delta y/2}\Big(\mathcal{F} H_z|^n_{i+1/2,j}\Big)\Big), \tag{49}$$

$$E_y|^{n+1}_{i,j+1/2} = \mathcal{F}^{-1} C\Big(\mathcal{F} E_y|^n_{i,j+1/2}\Big) - \Big(\mathcal{F}^{-1} iS\hat{k}_x e^{-ik_x \Delta x/2}\Big(\mathcal{F} H_z|^n_{i,j+1/2}\Big)\Big), \tag{50}$$

where known coefficients $C = \cos(\mathbf{k}c\Delta t)$ and $S = \sin(\mathbf{k}c\Delta t)$, and $\hat{\mathbf{k}} = [\mathbf{k}]/k$.

Note that the PSATD algorithm at order p is the limit of the FDTD algorithm at the same order p when $\Delta t \to 0$.

Although a time-leapfrogged version of PSATD exists [13], it is not of practical interest for usage in Particle-In-Cell simulations where both electric and magnetic components need to be explicitly known at the same time for pushing particles. Hence, we do consider only the time-centered version here, and thus only the coupling of PSATD with the PML-2SC algorithm.

4. Dispersion relation analysis of the PML, PML-2SS and PML-2SC

For simplicity, we restrict ourselves to the analysis of the dispersion relation of the normally incident monochromatic plane wave on the PML, PML-2SS and PML-2SC media with uniform conductivity across the domain ($\sigma_x = \sigma$, $\sigma_x^* = \sigma^*$ and $\sigma_y = \sigma_y^* = 0$). The PML, PML-2SS and PML-2SC equations can be rewritten as finite-difference equations of $\mathbf{E}$ or $\mathbf{H}$ only. After some algebraic manipulation, the following relations are obtained for the one-dimensional PML/PML-2SS formulation of arbitrary p-order:

$$E_y|_j^{n+1} = (\alpha + \alpha^*)E_y|_j^n - \alpha\alpha^* E_y|_j^{n-1} + \beta\beta^* \Delta_{k,m} E_y|_j^n, \tag{51}$$

and, for the PML-2SC formulation:

$$E_{y,j}^{n+1} = (\alpha + \alpha^*)E_y|_j^n - \alpha\alpha^* E_y|_j^{n-1} + \beta\beta^* \frac{(\alpha + \alpha^*)}{2} \Delta_{k,m} E_y|_j^n, \tag{52}$$

where $\Delta_{k,m} E_{y,j}^n = \sum_{k=1}^{p/2} \sum_{m=1}^{p/2} c_k^p c_m^p [E_y|_{j+k+m-1}^n - E_y|_{j+k-m}^n - E_y|_{j-k+m}^n + E_y|_{j-k-m+1}^n]$.

The derivation of the dispersion relation is based on the substitution of a monochromatic traveling plane-wave solution into the corresponding PML medium formulation. Assuming the propagation of a wave of the form $E_0 e^{i(\omega t - k_x x)}$, we obtain the dispersion relation valid for all abovementioned PML formulations and differing only by a set of coefficients (to be given below):

$$e^{2i\omega\Delta t} + b e^{i\omega\Delta t} + c = 0, \tag{53}$$

which gives an analytic representation of $\omega(k)$ in the form

$$\omega(k) = -\frac{i}{\Delta t} \ln\Big(\frac{-b \pm \sqrt{b^2 - 4c}}{2}\Big). \tag{54}$$

It should be noticed that the quadratic Eq. (53) offers two solutions. In our analysis, we use the positive sign solution and disregard the negative sign "parasitic" solution (see [18]). The PML's coefficients along with the coefficients of the quadratic Eq. (53) are given by:

- PML: $\alpha^{(*)} = e^{-\sigma^{(*)}\Delta t}$, $\beta^{(*)} = c\frac{1-e^{-\sigma^{(*)}\Delta t}}{\sigma^{(*)}\Delta x}$; $b = -(\alpha + \alpha^*) - \beta\beta^*\chi_{km}$, $c = \alpha\alpha^*$;
- PML-2SS: $\alpha^{(*)} = e^{-\sigma^{(*)}\Delta t}$, $\beta^{(*)} = c\frac{\Delta t}{\Delta x}$; $b = -(\alpha + \alpha^*) - \beta\beta^*\chi_{km}$, $c = \alpha\alpha^*$;
- PML-2SC: $\alpha^{(*)} = e^{-\sigma^{(*)}\Delta t}$, $\beta^{(*)} = c\frac{\Delta t}{\Delta x}$; $b = -(\alpha + \alpha^*)(1 + \beta\beta^*\chi_{km}/2)$, $c = \alpha\alpha^*$,

where $\chi_{km} = \sum_{k=1}^{p/2} \sum_{m=1}^{p/2} c_k^p c_m^p [e^{-ik\Delta x(k+m-1)} - e^{-ik\Delta x(k-m)} - e^{ik\Delta x(k-m)} + e^{ik\Delta x(k+m-1)}]$.

Figure 2 shows the real and imaginary parts of the 1-D dispersion relation solution of the PML, PML-2SS and PML-2SC formulations for different values of σ (uniform across the domain) and time steps, in the case of 2^{nd} and 32^{nd}-order PSTD operators.

With the PML-2SC formulation, the speed of waves does not change with σ and, as expected, we observe that $\Re[\omega(k)]$ is independent of σ while the damping $\Im[\omega(k)]$ increases with σ. In contrast, with the PML-2SS media, the speed of waves depends on the conductivity by construction (see Eqs. (10)-(11)), as observed in Fig. 2. We observe a slight dependence of the wave speed with σ with the standard PML algorithm. As expected, the damping $\Im[\omega(k)]$ is of the same order of magnitude in all cases, and proportional to σ.

Since the absorption efficiency of PMLs depends directly on the numerical dispersion properties that determine propagation and damping of waves, one would expect, based on these results, that the PML and PML-2SC implementations will have close absorption efficiencies.

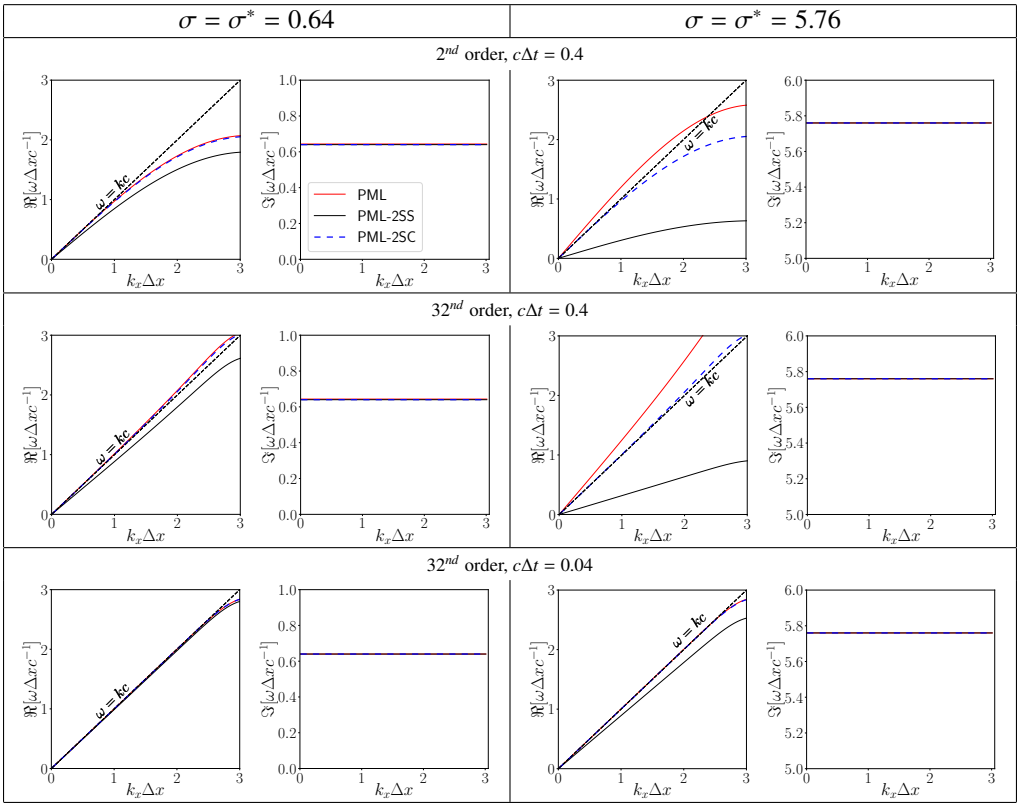

Figure 2: Real and imaginary part of the dispersion relation solution of the PML, PML-2SS and PML-2SC algorithms of the 2nd and 32nd orders, for different conductivities $\sigma = 0.64$ (left) and $\sigma = 5.76$ (right) and time steps, $c\Delta t = 0.4\Delta x$ (top and middle) and $c\Delta t = 0.04\Delta x$ (bottom).

5. Absorption Efficiency Analysis

In this section, we evaluate the absorption efficiency of the novel formulations of the PML and contrast to the absorption efficiency of the standard PML. The absorption efficiency is evaluated in two ways: (a) numerically via simulations, and (b) analytically using the "p-source" ("multi-source") analytical model, recently proposed in [16]. The "p-source" model enables an exact calculation of the total plane wave reflection coefficient, as it takes into account all multiple transmissions/reflections caused by each row/column of cells and considers all possible "secondary sources" that radiate, couple and contribute to the total reflection coefficient for any p-order stencil (see [16] for details).

5.1. Simulation Parameters

All numerical simulations have been performed on a 2-D uniform ($\Delta x = \Delta y$) staggered "Yee" grid of dimension $(N_x + 2N_{pml})\Delta x \times N_y \Delta y$ with time step $c\Delta t/\Delta x = 0.4$ (which is below the CFL condition in 1D, 2D and 3D for any order p). A schematic representation of the right-hand side of the simulation domain is shown in Fig. 1 (a). We assume that an EM signal is launched at the center of the simulation domain at $t = 0$, propagating in opposite directions at oblique incidence angle, φ. On the left and right boundaries of the simulation domain, a PML medium is set, while periodic boundary conditions (PBC) are applied on the upper and lower boundaries. Following [8], we used the quadratic PML's damping function given by:

$$\sigma_{xi} = \sigma_{max}\Big(\frac{i\Delta x}{\delta}\Big)^2, \;\; i = 0, .., N_{pml} \tag{55}$$

where $N_{pml} = 20$ is the depth of the APML medium (in terms of the number of cells), $\sigma_{max} = 4c/\Delta x$ and $\delta = 5\Delta x$. Since the $\mathbf{E}$ and $\mathbf{H}$ fields are staggered in space, the damping function σ^* is defined as $\sigma^* = \sigma_{i+1/2}$.

The incident signal is given by $H(t, \omega) = h(t)\sin(\omega t + yk_0 \sin\varphi)$, injected at a fixed wavenumber k_0 with a Harris function $h(t)$ temporal profile,

$$h(t) = \begin{cases} \frac{1}{32}\Big(10 - 15\cos(\frac{2\pi ct}{L}) + 6\cos(\frac{4\pi ct}{L}) - \cos(\frac{6\pi ct}{L})\Big), & \text{if } \; 0 < \frac{ct}{L} < 1 \\ 0, & \text{otherwise.} \end{cases} \tag{56}$$

Here, $\varphi = \arctan(k_y/k_x)$ is the incidence angle, c is the speed of light, ω is the angular frequency, given by the numerical dispersion relation of the chosen algorithm (given in Table A.1) and $L = 0.5N_x\Delta x$ is the distance along x axis from injection point to the APML. Because of the PBC at $y = 0$ and $y = N_y\Delta y$, we require the transverse wavenumber to be calculated as $k_y = 2\pi N/(N_y\Delta y)$ with $N \in \mathbb{N}$, while the longitudinal wavenumber is given by $k_x^2 = k_0^2 - k_y^2$. It should be noted that the Harris function is chosen for its quasi-monochromatic nature, which enables a precise evaluation of the reflection coefficient at a given frequency. The time-dependent amplitude of the Harris function along with its Fourier transform are given in Fig. 3.

The reflection coefficient of the TE plane wave striking the APML medium can be calculated as a ratio of the reflected field energy over the incident one,

$$R_{num}(\omega, t) = \sqrt{\frac{\sum_{i,j} |\mathbf{E}_{ij}^{inc}|^2 + c^2|\mathbf{B}_{ij}^{inc}|^2}{\sum_{i,j} |\mathbf{E}_{ij}^{ref}|^2 + c^2|\mathbf{B}_{ij}^{ref}|^2}}. \tag{57}$$

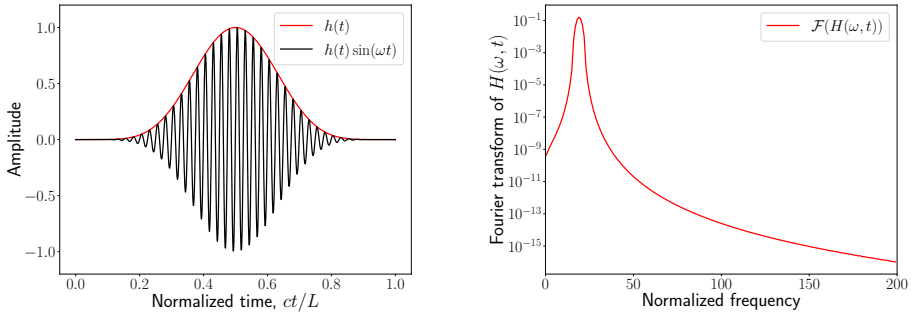

(a) (b)

Figure 3: (a) Amplitude of the Harris-like pulse $H(\omega, t) = h(t)\sin(\omega t)$ as a function of the normalized time, ct/L, and (b) its Fourier transform as a function of the normalized frequency.

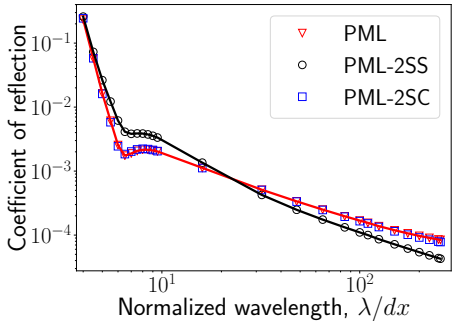

Figure 4: Comparison of the reflection coefficient as a function of the wavelength normalized by the cell size $\lambda/\Delta x$ of the PML, new PML-2SS and PML-2SC media at normal incidence, for a layer of depth 20, computed with an analytical "p-source" model (solid lines) and from simulations using the PSTD^2 (markers).

5.2. Normal incidence at order 2

Figure 4 shows the comparison of the reflection coefficient as a function of the normalized wavelength $\lambda/\Delta x$ for a plane wave striking a PML, PML-2SS or PML-2SC medium at normal incidence ($\varphi = 0$), computed with an analytical "p-source" model (solid lines) [16] and from simulations using the PSTD^2 method (markers).

The results confirm the predictions made from the numerical dispersion analysis above: the PML-2SC formulation has almost the same reflection coefficient as the standard PML at all wavelengths, while the PML-2SS differs (higher reflection at short wavelength and lower at long wavelength).

5.3. PML, PML-2SS, PML-2SC: Normal and Oblique Incidence at order 2, 8, 32, 64

Figure 5 shows plots of the reflection coefficient as a function of the wavelength of the incident wave normalized by the cell size $\lambda/\Delta x$ for a plane wave propagation in vacuum striking a PML, PML-2SS or PML-2SC medium at normal incidence, for a layer of depth 20, computed with an analytical "p-source" model (solid lines) [16] and from simulations using the PSTD^p method, for $p = 2, 8, 32, 64$. In order to emphasize the similarity between PML and PML-2SC

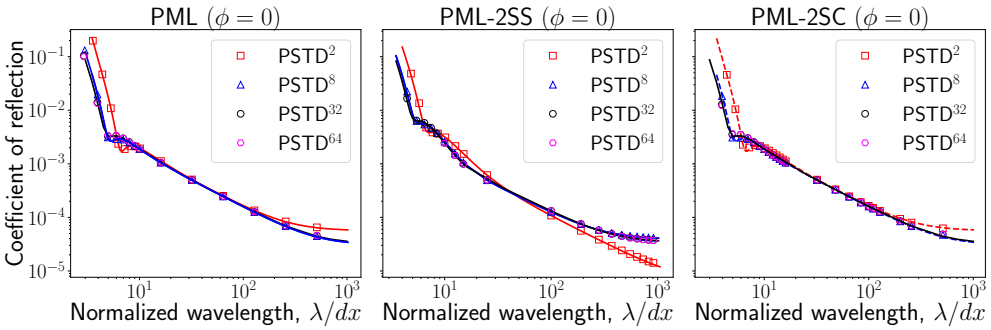

Figure 5: Reflection coefficient as a function of the normalized wavelength $\lambda/\Delta x$ of the PML, PML-2SS and PML-2SC media at normal incidence, for a layer of depth 20, computed with an analytical "p-source" model (solid lines) and from simulations (markers) using the PSTD^p method ($p = 2, 8, 32, 64$). PML-2SC numerical results are being compared together with analytical results of the PML "p-source" model (dashed lines).

media, PML-2SC numerical results are being shown together with analytical results of the PML "p-source" model (represented as dashed lines in Fig. 5 and Fig. 6).

In Fig. 6, the coefficient of reflection versus the plane wave incidence angle are given for fixed wavelengths, $\lambda/dx = 4$ (a) and $\lambda/dx = 8$ (b), respectively.

The results confirm that the PML-2SC has the same coefficient of reflection as the standard PML for any order, wavelength and angle of incidence, while the PML-2SS offers slightly different values.

5.4. PSATD PML-2SC: Normal and Oblique Incidence at order 2, 8, 32, 64

In this section, we explore whether the efficient absorption of the PML-2SC, which was observed in the previous section with second-order leapfrog time-stepping, holds when using subcycling, as well as at the limit of analytical time integration and infinite order of the PSATD algorithm.

In Fig. 7, we present the comparison between reflection coefficient of the PML-2SC, using the PSATD and high-order sub-cycled PSTD. The subcyling is applied during the first step of propagation in vacuum, while the second step of damping is unchanged. The notation PSTD$^p_{N_s}$ corresponds to the p-order PSTD method augmented with the sub-cycling in time of order N_s. The results show that the coefficient of reflection is largely insensitive to the order of the stencil and the amount of sub-cycling, up to the limit of infinite order and infinite subcycling. These results confirm that the new PML-2SC algorithm is an effective implementation of the PML algorithm with the PSATD solver.

6. Test of the new PML formulation in laser-plasma EM-PIC simulations

The new PML formulation has been first implemented in a very general form (using the interpreted programming language Python) in the WARP code [19], to easily account for any kind of Maxwell solvers (FDTD, PSATD^p, PSTD^p). Later, this general formulation was significantly accelerated in full FORTRAN (with shared memory parallelization) in the high-performance library PICSAR [20, 21] (abbreviated PXR below) jointly developed at LBNL and CEA. PXR

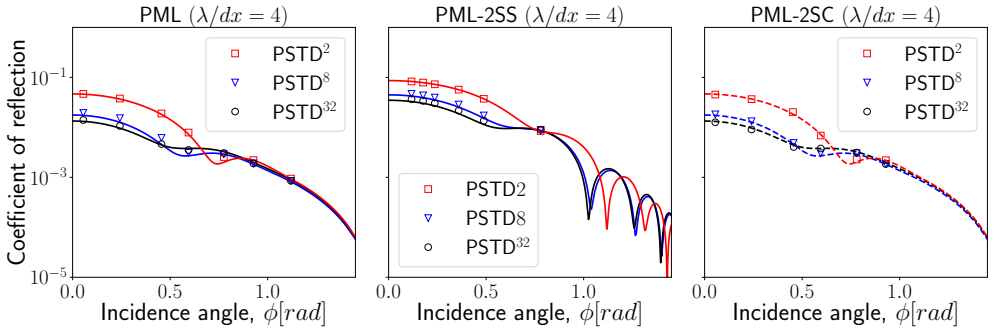

(a)

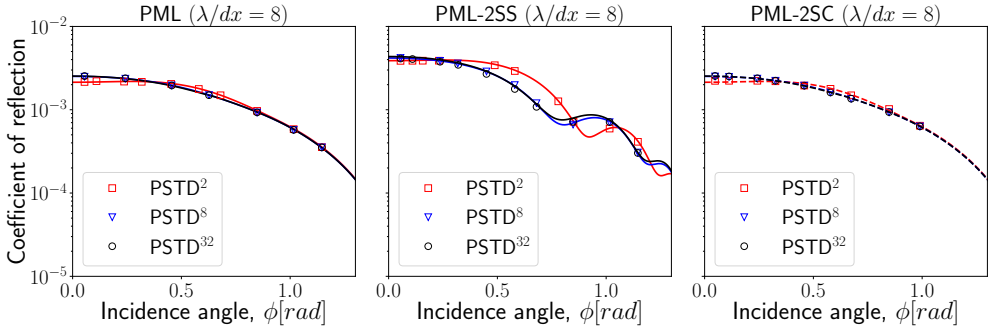

(b)

Figure 6: Reflection coefficient as a function of the plane wave incidence angle of the PML, PML-2SS and PML-2SC media for a fixed $\lambda/\Delta x = 4$ (a) and $\lambda/\Delta x = 8$ (b), for a layer of depth 20, computed with an analytical "p-source" model (solid lines) and from simulations (markers) using the PSTD^p method ($p = 2, 8, 32$). PML-2SC numerical results are being compared together with analytical results of the PML "p-source" model (dashed lines).

has been recently coupled to WARP and the resulting WARP+PXR capability is now routinely used at CEA Saclay to model laser interactions at ultra-high intensities with so-called relativistic plasma mirrors (initially made of solid targets) [4, 5].

Upon reflection of the high-intensity laser on the plasma mirror, the laser electric field makes the plasma surface oscillate at relativistic velocities, which in turn induces a periodic Doppler upshift of the reflected field associated to a high-order harmonic spectrum in Fourier space or a train of sub-femtosecond pulses in the time domain. These simulations are extremely challenging as they require a massively parallel implementation of ultrahigh-order pseudo-spectral PSATD^p solvers to mitigate spurious numerical dispersion effects over large bands of frequencies and angles [3]. Moreover, they require the use of highly efficient PMLs at each boundary of the simulation to:

- avoid spurious reflection of the high-intensity electromagnetic fields (incident and reflected fields) at the simulation domain boundaries, that could affect the plasma mirror dynamics or the propagation in vacuum of ejected particles (electrons, ions) from the plasma mirror surface. For the reflected field (consisting of high-order harmonics), the PML should ex-

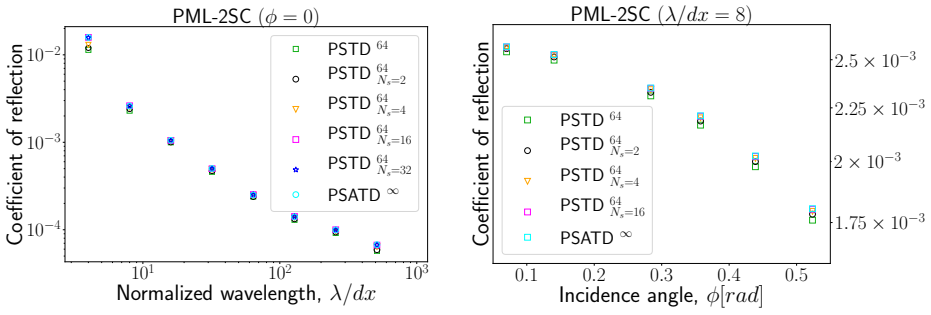

(a) (b)

Figure 7: Comparison of the reflection coefficient of the PML-2SC calculated via numerical simulation using PSATD$^{\infty}$, PSTD^{64} and PSTD$^{64}_{N_s}$ augmented with sub-cycling in time: (a) as a function of the normalized wavelength $\lambda/\Delta x$ at normal incidence and (b) as a function of the incidence for a fixed wavelength $\lambda/\Delta x = 8$.

hibit high efficiency for a large band of frequencies and angles. In this regard, notice that a good efficiency of the PMLs also allows for a significant reduction of the simulation box size (and thus time-to-solution),

- inject the laser field in the simulation box using an antenna. As the antenna emits two electromagnetic waves (one in the direction of the plasma mirror, the other one in the direction of the simulation boundary), PMLs are also needed to absorb the second undesired wave.

Fig. 8 presents results of a typical two-dimensional laser-plasma mirror simulation performed with WARP+PXR and the new PML formulation. Numerical and physical parameters are detailed in the caption of Fig. 8. The blue to red colormap represents the B_z field component orthogonal to the plane of incidence. Fig. 8 shows three snapshots of the magnetic field spatial profiles (B_z) at three different times:

1. at time $t = 5T$ when the antenna radiates the laser field (where T is the laser period). One can notice that the second "undesired" wave radiated by the antenna towards the left boundary is well absorbed by the PML without any spurious reflection,
2. at time $t = 36T$ when the laser field reflects off the plasma mirror surface (leading to harmonic generation in the reflected field),
3. at time $t = 79T$ when the reflected field approaches the right and upper boundaries. Here again, one can notice that the reflected field (containing a large harmonic content) is well absorbed by the PML.

Note however that when using high-order stencils, the boundaries for the electromagnetic fields need to be offset outwards from the particle boundaries to avoid spurious interaction of particles with the PML, potentially causing instabilities. In practice, using an offset of a few cells (as in the present simulation) rapidly mitigates this instability, which consequently does not require any special treatment.

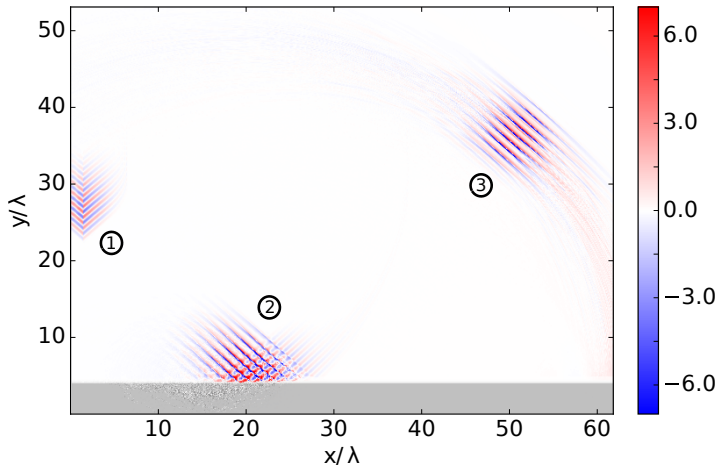

Figure 8: Simulation of laser-plasma mirror interaction at ultra-high intensity. The blue-to-red colormap represents the B_z field component at three different times $5T$, $36T$ and $79T$ (labelled 1, 2, 3) where T is the laser period. The gray colormap represents a snapshot of the plasma mirror electron density (at time of label 2). **Physical parameters:** the p-polarized laser (TE mode) hits the plasma mirror at oblique incidence $\theta = 45^o$ in the (x, y) plane. The laser normalized amplitude $a_0 = eE_0/m_e\omega c$ is 6, where E_0 is the laser electric field amplitude, ω the laser frequency, c the speed of light and m_e the electron mass. The plasma mirror has an exponential electron/ion density profile $n_e \propto \exp(x/L)$, where $L = \lambda/8$ is the gradient scale length and λ the laser wavelength. The electron density profile plateaus at $100n_c$ with $n_c(\omega)$ being the plasma critical density associated to the laser frequency ω. **Numerical parameters**: the simulation box dimension is $50\lambda \times 40\lambda$ with a spatial resolution of $\delta x = \delta z = \lambda/100$. Time step is chosen so that $c\delta t = \delta z$. PSATD^p solver is used with $p = 100$. PMLs are appended to all simulation boundaries. The plasma is initially cold.

7. Conclusions

This paper introduced a novel "two-step" formulation in progressive steps, starting from the standard FDTD discretization, then applying to arbitrary-order solvers and pseudo-spectral time-domain, and finally to pseudo-spectral analytical time-domain solvers. Two implementations were proposed: time-staggered "PML-2SS" and time-centered "PML-2SC". Analysis of the numerical dispersion of the new formulations showed that the PML-2SC's velocity and damping rates are nearly identical to those of the standard PML, while the PML-2SS's is somewhat different. This is confirmed further by the analytical and numerical estimations of absorption rates, where it is found that the PML-2SC's absorption rate is nearly identical to Berenger's PML at all wavelength and angle. It is also demonstrated that the efficiency of the PML-2SC is preserved at any order, including at the limit of infinite order, validating the applicability of PML-2SC with the PSATD Maxwell solver. The new PML formulation was successfully implemented in a PIC code and applied to the challenging modeling of plasma mirrors. This study was restricted to the extension of the split formulation of the PML to PSATD. Further studies will examine the applicability to unsplit formulations.

8. Acknowledgements

The authors are grateful to Maxence Thevenet and Remi Lehe for many helpful discussions.

This research was supported by the Exascale Computing Project (ECP), Project Number: 17-SC-20-SC, a collaborative effort of two DOE organizations—the Office of Science and the

Table A.1: 3D numerical dispersion relation and CFL conditions for FDTD, PSTD and PSATD schemes of arbitrary order.

Method	Numerical Dispersion Relation	CFL condition
FDTD^p/PSTD^p	$\left[\frac{1}{c\Delta t}\sin\left(\frac{\omega\Delta t}{2}\right)\right]^2 = \sum_u \left[\frac{1}{\Delta u}\sum_{l=1}^{p/2} c_l^p \sin\left((2l-1)k_u\Delta u/2\right)\right]^2$	$c\Delta t \leq \Delta_{xyz}/\sum_{l=1}^{p/2}\lvert c_l^p\rvert$
PSTD$^\infty$	$\sin(\omega\Delta t/2) = kc\Delta t/2$	$c\Delta t \leq 2\Delta_{xyz}/\pi$
PSATD^p	$(\omega/c)^2 = \sum_u \left[\frac{1}{\Delta u}\sum_{l=1}^{p/2} c_l^p \sin\left((2l-1)k_u\Delta u/2\right)\right]^2$	Free of CFL
PSATD$^\infty$	$(\omega/c)^2 = k^2$	Free of CFL

Table notations: $\Delta_{xyz}^{-1} = \sqrt{1/\Delta x^2 + 1/\Delta y^2 + 1/\Delta z^2}$, $\sum_u = \sum_x + \sum_y + \sum_z$ and $k^2 = \sum_u k_u^2$.

National Nuclear Security Administration—responsible for the planning and preparation of a capable exascale ecosystem—including software, applications, hardware, advanced system engineering, and early testbed platforms—to support the nation's exascale computing imperative.

This work was supported in part by the Director, Office of Science, Office of High Energy Physics, U.S. Dept. of Energy under Contract No. DE-AC02-05CH11231. An award of computer time (PICSSAR_INCITE) was provided by the Innovative and Novel Computational Impact on Theory and Experiment (INCITE) program. This research used resources of the Argonne Leadership Computing Facility, which is a DOE Office of Science User Facility supported under Contract DE-AC02-06CH11357.

Appendix A. Numerical Dispersion Relation Analysis of the FDTD, PSTD and PSATD algorithms

The accuracy and stability of the arbitrary-order FDTD, PSTD and PSATD discretization schemes are studied by substituting the plane monochromatic traveling-wave trial solutions into the corresponding discretized forms of the Maxwell's equations. In Table A.1, the corresponding 3-D numerical dispersion relations of the EM waves in vacuum along with the CFL conditions are summarized for the various schemes.

References

[1] K. Yee, IEEE Transactions On Antennas And Propagation Ap14 (3) (1966) 302–307.

[2] M. Karkkainen, E. Gjonaj, T. Lau, T. Weiland, in: Proc. Of International Computational Accelerator Physics Conference, Chamonix, France, 2006, pp. 35–40.

[3] G. Blaclard, H. Vincenti, R. Lehe, J. L. Vay, Physical Review E 96 (3) (2017) 033305. doi:10.1103/PhysRevE.96.033305, [link].
URL https://link.aps.org/doi/10.1103/PhysRevE.96.033305

[4] A. Leblanc, S. Monchocé, H. Vincenti, S. Kahaly, J.-L. Vay, F. Quéré, Phys. Rev. Lett. 119 (2017) 155001. doi:10.1103/PhysRevLett.119.155001, [link].
URL https://link.aps.org/doi/10.1103/PhysRevLett.119.155001

[5] H. Vincenti, J.-L. Vay, Computer Physics Communicationsdoi:https://doi.org/10.1016/j.cpc.2018.03.018, [link].
URL http://www.sciencedirect.com/science/article/pii/S0010465518300900

[6] Q. Liu, Microwave And Optical Technology Letters 15 (3) (1997) 158–165. doi:10.1002/(Sici)1098-2760(19970620)15:3¡158::Aid-Mop11¿3.3.Co;2-T.

[7] I. Haber, R. Lee, H. Klein, J. Boris, in: Proc. Sixth Conf. Num. Sim. Plasmas, Berkeley, Ca, 1973, pp. 46–48.

[8] J. Berenger, Journal of Computational Physics 114 (2) (1994) 185–200.

[9] J. Berenger, Journal of Computational Physics 127 (2) (1996) 363–379.

[10] Y. Ohmura, Y. Okamura, Piers Online 6 (7) (2010) 632–635.

[11] J.-L. Vay, Journal of Computational Physics 165 (2) (2000) 511–521. [link].
URL http://www.sciencedirect.com/science/article/pii/S0021999100966233

[12] J.-L. Vay, Journal of Computational Physics 183 (2) (2002) 367–399. [link].
URL http://linkinghub.elsevier.com/retrieve/pii/S0021999102971755

[13] J. L. Vay, I. Haber, B. B. Godfrey, Journal of Computational Physics 243 (2013) 260–268.

[14] B. Fornberg, SIAM Journal on Numerical Analysis 27 (4) (1990) 904–918. doi:10.1137/0727052.

[15] I. R. Khan, R. Ohba, Journal of Computational and Applied Mathematics 107 (2) (1999) 179–193. doi:10.1016/s0377-0427(99)00088-6.

[16] H. Vincenti, J.-L. Vay, Computer Physics Communications 200 (2016) 147–167. doi:10.1016/j.cpc.2015.11.009.

[17] J. M. Dawson, Reviews Of Modern Physics 55 (2) (1983) 403–447. doi:10.1103/RevModPhys.55.403.

[18] B. Gustafsson, H.-O. Kreiss, J. Oliger, Time Dependent Problems And Difference Methods, Wiley, 1995.

[19] Warp, http://blast.lbl.gov/blast-codes-warp.
URL http://blast.lbl.gov/blast-codes-warp

[20] H. Vincenti, M. Lobet, R. Lehe, R. Sasanka, J.-L. Vay, Computer Physics Communications 210 (2017) 145 – 154.

[21] J. L. Vay, I. Haber, B. B. Godfrey, Journal of Computational Physics 243 (2013) 260–268.

[22] P. Lee, J.-L. Vay, Computer Physics Communications 194 (2015) 1–9. doi:http://dx.doi.org/10.1016/j.cpc.2015.04.004, [link].
URL http://www.sciencedirect.com/science/article/pii/S0010465515001356

[23] H. Vincenti, M. Lobet, R. Lehe, J. Deslippe, J.-L. Vay, Exascale scientific applications: scalability and performance portability, Chapman & Hall/CRC, 2017.

[24] PICSAR, https://www.picsar.net.
URL https://www.picsar.net